Materials Advances

ROYAL SOCIETY OF CHEMISTRY

PAPER

View Article Online
View Journal | View Issue

Cite this: *Mater. Adv.*, 2026, 7, 2690

Enhancing durability of Pt-coated titanium porous transport layers for PEM water electrolysis using TiN interlayers

Muhammad Azhar Iqbal, Sukhvant Singh, Aditya Singh and Samaneh Shahgaldi *

The durability and efficiency of proton exchange membrane water electrolysers (PEMWEs) are influenced by multiple factors, particularly the stability of platinum (Pt) coated porous transport layers (PTLs), which degrade under acidic and oxidative environments. TiO_x passivation during anodic polarization increases interfacial resistance and reduces electrochemical performance. To address this issue, this study explores the use of a titanium nitride (TiN) interlayer, deposited *via* reactive magnetron sputtering, to enhance the stability of Pt-coated titanium felt (Ti-felt) PTLs. Pt layers are deposited by varying sputtering power, and TiN interlayers with varying thickness are applied beneath the best-performing Pt layer. Electrochemical corrosion testing, long-term chronoamperometry (1 A cm^{-2} in 0.5 M H_2SO_4), and *in situ* PEMWE single-cell evaluations show that the sample with the 400 nm TiN interlayer exhibits the lowest corrosion current (39.26 μA cm^{-2}), improved charge transfer resistance (3552 Ω cm^2), and structural integrity. Additionally, the TiN interlayer extended the Pt-coated PTL durability by 80 hours, significantly reducing interfacial degradation and offering a promising strategy for long-lasting high-efficiency PEMWE systems.

Received 27th November 2025,
Accepted 14th January 2026

DOI: 10.1039/d5ma01378j

rsc.li/materials-advances

Introduction

Global hydrogen (H_2) demand in 2024 surpassed that in 2023 (97 Mt) with a 2% increase and is projected to cross 100 million tons in 2025. Clean hydrogen demand grew by 10% in 2024, marking a significant contribution toward the ambitious net zero targets for 2050. The aim is to increase the demand to 37 million tons per year by 2030.[1,2] This urgent transition toward sustainable and clean energy solutions has intensified the focus on hydrogen as a pivotal energy carrier, mainly green hydrogen.[3,4] The U.S. Department of Energy has launched the "Hydrogen Shot" program to reduce the cost of clean hydrogen to $1 per kilogram within a decade. This highlights the strategic importance of advanced cost-effective and scalable hydrogen production technologies.[5] In conjunction with the global decarbonisation efforts, hydrogen has emerged as a pivotal component for net zero targets and a versatile energy carrier across sectors.[6,7] Among various H_2 production technologies, Polymer Electrolyte Membrane Water Electrolysis (PEMWE) is recognised for its high efficiency, fast response time, and compatibility with intermittent renewable energy sources.[8–10] PEMWE is designed around the membrane electrode assembly (MEA). The PTL at the anodic side is crucial for water transport, electron conduction, oxygen removal, as well as a mechanical support between the catalyst layer (CL) and flow fields.[11–15] Typically, titanium fulfils the requirements of PTLs through its excellent conductivity and corrosion resistance characteristics under acidic and oxidising conditions.[16] However, titanium forms a passivating oxide layer, especially under sustained positive potentials. Thus, increasing the interfacial resistance and compromising system performance.[17–21] The deterioration of Ti-PTL is further aggravated by the strong acidic environment (pH < 1) and high anodic potentials (>1.4 V *vs.* RHE) experienced during the OER in PEMWE. The combined effect of low pH and oxidative stress promotes the formation of insulating titanium oxides and surface instability, particularly at defect sites. To combat these challenges, different corrosion resistance and conductive coatings such as iridium (Ir), platinum (Pt), gold (Au), niobium nitride (NbN), and IrPt have been explored.[8,20,22–28] PTLs contribute about 32% of the total stack cost,[29] and commercial Ti-PTLs use a thick (200 nm) Pt coating.[30] Noble metals enhance conductivity and durability but significantly increase the capital costs of PEMWE. Consequently, recent research has thus been directed to minimizing the use of noble metals through different strategies such as exploring cost-effective alternatives, optimising the coatings, and investigating alloy and interlayer schemes.[18,31–35] Particularly, one promising approach involves nitride-based coatings. TiN offers excellent corrosion resistance, conductivity, and mechanical durability, making it suitable for harsh anodic conditions in PEMWE.[36–39]

Hydrogen Research Institute, Université du Québec à Trois-Rivières, Trois-Rivières, Québec G8Z 4M3, Canada. E-mail: Samaneh.Shahgaldi@uqtr.ca

Daudt *et al.* demonstrated that NbN coatings improved the corrosion resistance and surface stability of Ti PTLs for PEMWE.[18] Ye *et al.* investigated reactively sputtered Ta, Cr and Tb nitride coatings on Ti bipolar plates for PEMWE, and comparative analysis showed the TaN coating achieved the lowest corrosion current and enhanced the cell efficiency by 6.37%.[40] Likewise, TiN is a conductive ceramic that serves as an effective protective barrier to suppress titanium oxidation and maintain low interfacial contact resistance.[41] Additionally, TiN is well-reported for fuel cell applications to enhance bipolar plate performance.[39,42–45] For polymer electrolyte membrane fuel cells (PEMFCs), Wang *et al.* employed high-power impulse magnetron sputtering (HiPIMS) to develop TiN coatings on titanium plates, achieving improved surface compactness and reduced porosity by adjusting the N_2 flow rate.[46] Optimised TiN coatings can prevent electrolyte penetration and minimise localised degradation. Therefore, tuning deposition parameters and coating thickness is essential to develop dense and uniform films and thus optimal corrosion resistance.[46] While TiN can provide significant protection against the passive oxidation of titanium by forming a compact diffusion barrier and corrosion-resistant interlayer,[37] its limited catalytic activity toward the oxygen evolution reaction (OER) necessitates a conductive, catalytically active top layer. A thin Pt layer is thus desired over TiN to leverage high stability and conductivity, while TiN suppresses titanium oxide formation and enhances Pt adhesion. This bilayer configuration ensures interfacial stability and corrosion protection under acidic anodic conditions, which are critical for long-term PEMWE performance.[41,47,48] Magnetron sputtering is a scalable and industry-relevant technique commonly employed for protective coatings in electrochemical systems such as fuel cells and water electrolysers.[49–51] Among its key process parameters, sputtering power has a significant influence on the microstructure and surface morphology of the deposited films. Higher sputtering power increases the energy of sputtered atoms, enhancing surface diffusion, atomic rearrangement, and densification. Conversely, excessive power may promote grain growth and localised agglomeration, potentially introducing internal stress or surface defects. These structural variations directly affect film stability in electrochemical environments.[52] Therefore, tuning the sputtering parameters is essential to achieve the desirable structural features that enhance the durability and interfacial stability of porous transport layers in PEMWE systems. To the best of the authors' knowledge, this Pt/TiN bilayer on Ti-felt PTLs has not yet been explored in the context of PEMWE systems. Motivated by this gap, the presented study focuses on evaluating the efficacy of TiN as an interlayer in Pt-coated Ti-felt as the PTL in PEMWE. The study involved the development of Pt coatings through DC sputtering at varying deposition powers, followed by physical and electrochemical characterisations. The optimal Pt coating was used as the top layer in a series of samples incorporating reactive DC magnetron sputtered TiN interlayers of varying thicknesses (100, 400, and 700 nm) to systematically evaluate the role of TiN for enhanced corrosion resistance and interfacial stability. Subsequently, these samples were evaluated under simulated PEMWE conditions through half-cell testing followed by single cell testing using a commercial membrane electrode assembly (MEA) to assess the polarisation behaviour and interfacial characteristics.

Materials and methods

Cleaning of the Ti-felt substrate

This study utilised a commercially sourced Bekipor ST from Bekaert, a Ti-felt substrate characterised by a thickness of 250 μm and a porosity of 68%. Before each deposition experiment, the substrates underwent a cleaning process. This involved rinsing in deionised water, an ultrasonic bath in acetone for 15 min, and immersion in 35% hydrochloric acid (HCl) solution at 53 °C for 2 min to eliminate any superficial oxide layers, followed by two successive rinses in deionised water.[53,54] After rinsing, the substrates were dried in a vacuum furnace at 70 °C for three hours. The experimental work was divided into two main phases: firstly, the development of the Pt coatings at different sputter powers, and secondly, the evaluation of three different layers of the TiN interlayer under the best performing Pt coating conditions.

Pt coatings

Pt coatings were prepared using a 99.99% pure Pt target on a DC magnetron sputtering gun, Fig. 1(a). The pre-cleaned Ti-felt samples were placed in a high-vacuum chamber maintained at 5×10^{-6} Torr. The substrate holder was positioned 14 mm below the sputtering target and set to rotate at a constant speed of 5 rpm throughout the deposition process to ensure uniform film coverage. Argon was introduced into the chamber as a working gas, and the sputtering was conducted at 4×10^{-3} Torr. The deposition process was repeated to coat both sides of the samples. Three sets of samples were prepared at 60 W,

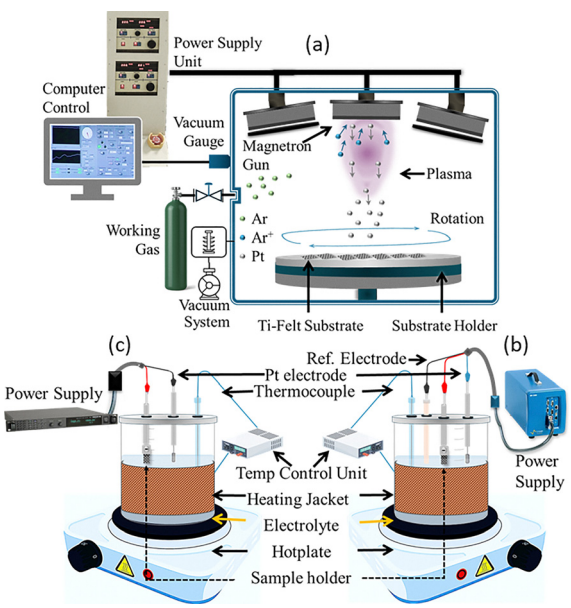

Fig. 1 (a) DC magnetron sputtering setup of the Pt coating, (b) electrochemical testing setup, and (c) end of life testing setup.

Table 1 Sputter deposition parameters

Material	Parameters	Values
Pt	Base pressure	5×10^{-6} Torr
	Substrate temp	25 °C
	Working pressure	4×10^{-3} Torr
	Power	60, 120 and 240 W
	Coating time	10 min
TiN	Base pressure	4×10^{-7} Torr
	Substrate temp	150 °C
	Substrate rotation	5 rpm
	Gas pressure	5 mTorr
	Ratio (Ar : N) (%)	80 : 20
	Working pressure	4×10^{-3} Torr
	Substrate bias	30 V
	Power	350 W

120 W, and 240 W sputtering power, while the coating time (10 min) was kept constant. Table 1 details all the processing parameters. Additionally, a thin titanium (Ti) layer (150 W for 5 min) was deposited as an interlayer in all the Pt coating experiments to enhance the adhesion.

TiN coatings

Reactive DC magnetron sputtering (RDCMS) is recognised as a robust method to obtain high-quality, well-adhered TiN films.[38,55] Ti-felt samples were loaded in a high vacuum chamber, where the base pressure reached 4×10^{-7} Torr using a turbomolecular pump backed by a rotary vane pump. The working gas pressure was maintained at 5 mTorr with an $Ar : N_2$ ratio of 80 : 20, controlled precisely by mass flow controllers under a working pressure of 4×10^{-3} Torr. Three TiN thicknesses—100, 400, and 700 nm were deposited using 99.99% pure Ti target *via* RDCMS. Film thickness was estimated using the Quartz Crystal microbalance. Prior to the deposition, substrates were pre-cleaned using argon plasma for 15 min at 50 W and 7 mTorr of Ar pressure to eliminate any potential titanium oxide (TiO_x) impurities. The coating process parameters are given in Table 1. Subsequently, the selected Pt topcoat (120 W sputter power for 10 min) was deposited onto the TiN-coated samples using the identical chamber configuration from the initial experimental series.

Physical characterisation

The surface morphology of Pt and TiN-coated samples was examined using a scanning electron microscope (SEM) to investigate the influence of different sputter parameters. Additionally, crystallographic profiles of the coatings were analysed with a PANalytical X'Pert PRO MRD X-ray diffractometer operated in grazing incident mode using Cu Kα radiation (λ = 0.1454 nm). The incident angle was set at 3°, with a 2θ range from 20 to 80 degrees.

Electrochemical characterisation

To assess the corrosion resistance of the coatings, both potentiostatic and potentiodynamic polarisation techniques were employed. The experimental configuration utilized a Biologic SP300 Potentiostat equipped with a three-electrode system. This setup included a saturated Hg/Hg_2SO_4 reference electrode, a Pt counter electrode, and the coated PTL as the working electrode (Fig. 1(b)). The electrolyte was a 0.5 M sulfuric acid (H_2SO_4) solution, maintained at 70 °C. The exposed geometric area of each test sample was standardised at 1.0 cm^{-2}. All measured potentials were initially recorded *versus* the Hg/Hg_2SO_4 reference and subsequently converted to the reversible hydrogen electrode (RHE) scale using the relationship: $E_{RHE} = E_{Hg/Hg_2SO_4} + 0.640 + (0.059 \times 0.024)$.[56,57] Electrochemical techniques were designed to comprehensively understand performance under controlled conditions. The scheme began with an open circuit voltage (OCV) stabilisation phase to allow the system to equilibrate with the potential monitored at a sampling interval of 0.5 seconds. Following this, a Tafel polarisation analysis was conducted to evaluate the corrosion kinetics, involving a potential sweep from −0.3 V to 1.35 V *vs.* the reference electrode at a scan rate of 1 mV s^{-1}. Potentiostatic Electrochemical Impedance Spectroscopy (PEIS) was then employed to study the interfacial and charge-transfer properties of the material across a frequency range of 200 kHz to 50 mHz, using a 10 mV AC perturbation relative to the open circuit potential. The impedance spectra were analyzed using EC-Lab software (BioLogic) to extract parameters from the equivalent circuit model. To ensure reproducibility, all EIS measurement was performed in triplicate (Fig. S2) and Kramers–Kronig consistency was conducted using the LIN-KK tool. The residuals in the range of 0.2 to 0.5% confirmed the linearity and stability of all spectra (Fig. S3 and S4).[58,59] Chronoamperometry (CA) was subsequently conducted by maintaining a constant potential of 1.35 V *vs.* the reference electrode for 15 hours, with transient current responses recorded to capture dynamic behaviour and total charge transfer.

End-of-life testing

To evaluate the long-term durability of the coated PTL, a stability test was conducted. This involved immersing the coated sample in a 0.5 M H_2SO_4 solution. The electrolyte was maintained at 70 °C using a heating pad wrapped around the beaker, connected to an automatic temperature controller with a feedback thermocouple immersed in the solution. Before mounting the sample, the setup was stabilized for 30 min to ensure a uniform temperature profile. Testing was conducted at a current density of 1 A cm^{-2} using a BK Precision DC power supply in a two-electrode configuration: the coated sample as the working electrode and Pt coil as the counter electrode, as illustrated in Fig. 1(c). Moreover, the sample holder was adjusted so that only 1 cm^2 area of sample was dipped in the electrolyte. Voltage variations were continuously monitored over time at a constant current. The sharp increase in voltage indicates sample failure.[60]

In situ testing: performance evaluation using a PEMWE single cell

The *in situ* single-cell performance was assessed using an E30 Greenlight Innovation Inc. electrolyser test station. The coated Ti-felt PTL samples were mounted on the anode side of a 5 cm^2 Scribner Electrolysis Cell assembly, accompanied by a commercial (Ion Power) Nafion 115 membrane electrode assembly

(MEA) with 1.0 mg cm^{-2} IrO_x at the anode and 0.5 mg cm^{-2} Pt/C at the cathode. The cell temperature was maintained at 70 °C using a heated water system. The anode utilised a Pt-coated Ti bipolar plate with a serpentine flow field. While at the cathode, a graphite BP plate with an identical flow field and a carbon fiber paper gas diffusion layer (GDL) (AvCarb GDS3250, 225 μm) was used. The PEMWE cell assembly incorporated 250 μm PTFE gaskets, with a uniform torque of 8 Nm applied to each of the eight bolts to ensure optimal sealing. Deionised water was supplied to the anode at 50 mL min^{-1}. Conditioning involved applying sequential current densities from 0.2 to 1.0 A cm^{-2}, with each level maintained for 30 min. Following this, polarization measurements were obtained by gradually increasing the current density from 0 to 2.0 A cm^{-2}. Electrochemical impedance spectroscopy (EIS) was subsequently performed at fixed current densities of 0.4, 0.8, 1.2, 1.6, and 2.0 A cm^{-2}, spanning a frequency range of 100 kHz to 0.1 Hz.

Results and discussion

Microstructure and morphology of Pt coatings

SEM micrographs (Fig. 2) reveal noticeable morphological variations among Pt-coated Ti-felt samples corresponding to differences in sputtering power. As the sputtering power increases, the deposition rate and film thickness are expected to rise, leading to a more uniform and complete coverage of the Ti-felt fibers. At 60 W (Fig. 1(a)), the deposited films exhibit a cauliflower-like grain morphology with open grain boundaries. Low sputtering power results in the ejection of smaller grains with lower kinetic energy, leading to incomplete surface coverage. In contrast, coatings deposited at 120 W (Fig. 2(b)) present a smoother morphology, with high-magnification images revealing reduced grain boundaries. This can be attributed to the coalescence of small and large grains, which interlock and overlap to form a compact and uniform structure with minimal uncovered regions. At 240 W, the film presents larger grains with a more isolated structure, yet the grain boundaries appear more distinct and regular. The increase in grain size at higher sputtering power suggests enhanced adatom mobility, which promotes grain growth and boundary refinement.[61,62]

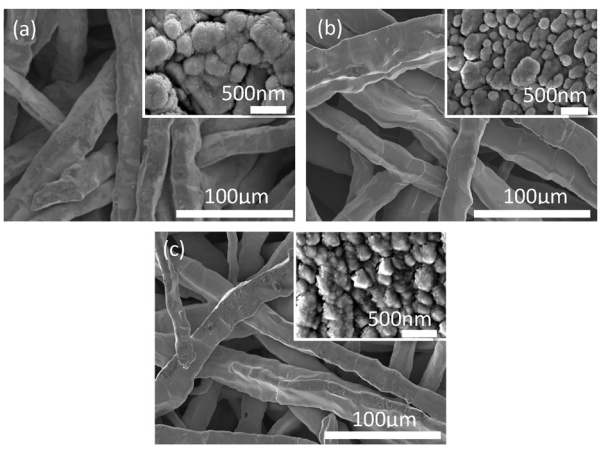

Fig. 2 SEM images of Pt-coated Ti-felt (a) Pt 60 W, (b) Pt 120 W, and (c) Pt 240 W.

Fig. 3 illustrates the XRD patterns of Pt-coated Ti samples processed under varying power levels. The diffraction peaks corresponding to the (111), (200), (220), and (311) crystal planes are attributed to Pt (PDF No. 04–0802), while the remaining peaks are associated with the Ti-felt substrate matching with Ti (PDF No. 044-1294). As the sputter power increased, the intensity of the Pt diffraction peaks became more pronounced, whereas the substrate peaks diminished, suggesting a progressive increase in coating thickness. The Pt (111) diffraction peak exhibits the highest intensity among the observed peaks. Furthermore, all diffraction peaks intensify with increasing power, highlighting an improved crystallinity. Moreover, a slight shift in the Pt diffraction peaks was observed, which can be attributed to the presence of strain within the crystal lattice. The strain and crystallite size were quantified using the Williamson–Hall (WH) method (eqn (1)).[62,63]

$$\beta\cos(\theta) = k\lambda/D + 4\varepsilon\sin(\theta) \quad (1)$$

where β is the full width at half maximum (FWHM) of the peak, θ is the Bragg angle, k is the shape factor, typically $\sim$0.9, λ is the X-ray wavelength, D is the crystallite size (nm), and ε is the micro-strain. Eqn (1) is the uniform deformation model, which can be treated as a linear equation. To calculate the crystallite size (D) and micro strain (ε), a WH plot is constructed by plotting $\beta\cos\theta$ against $4\sin\theta$ as detailed in the supplementary information (Fig. S1). The slope of the resulting line provides the microstrain, while the intercept gives the crystallite size, which can be derived using the equation $D = K\lambda/\beta\cos\theta$.

Table 2 details the crystallite size and strain percentage of the Pt coatings determined using the WH method. The

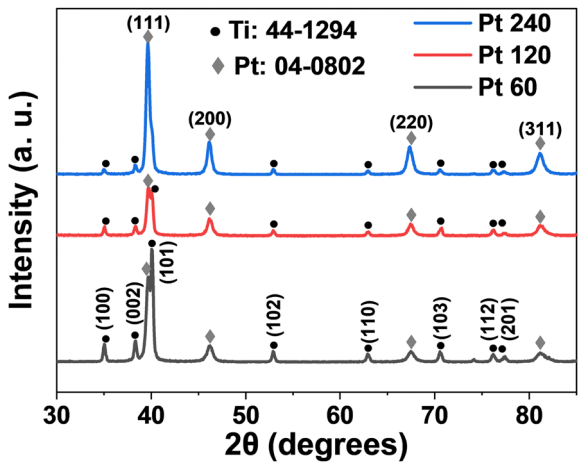

Fig. 3 XRD pattern of Pt-coated Ti-felt.

Table 2 Crystallite size and strain calculated by the W–H method

Sample	Crystallite size (nm)	% strain
Pt-60	15.58	0.051
Pt-120	18.99	0.058
Pt-240	33.01	0.193

Table 3 Equivalent circuit model parameters for PEIS analysis of Pt-coated Ti-felt

Sample	R_s (Ω cm^2)	R_{ct} (Ω cm^2)	R_{pfc} (Ω cm^2)
Pt-60	1.007	1390	382.9
Pt-120	0.813	3298	1683.0
Pt-240	0.8844	2973	518.5

calculated crystallite sizes show a clear dependence on sputtering power: Pt-60 exhibits the smallest crystallite size of 15.58 nm, while Pt-120 and Pt-240 show larger sizes of 18.99 nm and 33.01 nm, respectively. Increasing crystallite size with sputtering power suggests enhanced atomic mobility at higher energies, encouraging grain growth and improved crystalline quality. Concurrently, the strain percentages reveal an opposite trend. Pt-60 and Pt-120 demonstrate nearly zero strain, 0.051% and 0.058%, respectively. Meanwhile, Pt-240 exhibits more tensile strain (0.193%). This can be attributed to the larger grains and the resulting internal stresses from lattice mismatch and thermal expansion effects during deposition, which are more pronounced in thicker films.[64]

Corrosion performance of Pt-coated Ti-felt PTLs

The Open Circuit Voltage (OCV) represents a material's inherent electrochemical stability in an electrolytic environment. A more noble and stable OCV indicates enhanced corrosion resistance.[8,65] The stabilised OCV values of Pt-coated Ti-felt samples reveal distinct variations with sputtering power, with Pt-60 stabilising at 0.850 V, Pt-120 at 0.872 V, and Pt-240 at 0.893 V, as shown in Fig. 4(a). Pt-240 exhibits the highest OCV, which usually refers to a dense morphology with a more stable surface potential. However, superior corrosion resistance is not solely dictated by OCV trends. For further investigation, the Tafel polarisation analysis (Fig. 4(b)) provides a more direct assessment of corrosion kinetics. The magnitude of corrosion current (I_{corr}) serves as a direct indicator of the corrosion rate: a lower I_{corr} denotes a diminished corrosion rate, thus superior corrosion resistance of the material.[39] Pt-120 demonstrates a corrosion potential (E_{corr}) of 0.913 V and the lowest I_{corr} (41.1 μA cm^{-2}). These values suggest that Pt-120 possesses the most effective barrier properties against electrochemical degradation, owing to its compact surface morphology formed with the distribution of small and large grains, outperforming Pt-60 (0.9103 V and 42.2 μA cm^{-2}) and Pt-240 (0.926 V and 47.7 μA cm^{-2}). The Pt-240 sample, despite its high OCV, does not exhibit the lowest I_{corr}, suggesting that the high sputtering power introduces residual stress and unfavorable structural features such as grain coarsening that accelerate localised corrosion processes. This observation aligns with the SEM image (Fig. 2(c)), showing open grain boundaries, and with the XRD results, indicating the largest crystallite size (33.01 nm) and highest strain (0.193%). Furthermore, potentiostatic electrochemical impedance spectroscopy (PEIS) assessed the electrochemical properties of Pt-coated Ti-felt. As illustrated in Fig. 4(c), the Nyquist plots reveal distinct semicircular responses. The diameter of the semi-circle is in the order Pt-120 > Pt-240 > Pt-60, representing the highest capacitive performance of Pt-120. The accompanying inset delineates the equivalent circuit modelling of EIS data and high frequency impedance response. Key circuit components included the solution resistance (R_s), double-layer capacitance (C_{dl}), and charge transfer resistance (R_{ct}), which together characterize the effectiveness of the interfacial barrier between the Ti PTL and the acidic electrolyte. Additional factors, such as the constant phase element (CPE), reflect the surface heterogeneity, and the protective film corrosion resistance (R_{pfc}) represents the resistance offered by the protective layer against corrosive degradation, thereby reflecting its integrity (Table 3). The Pt-120 sample exhibits the highest R_{ct} (3298 Ω cm^2), suggesting superior corrosion resistance due to a densely packed and well-adhered coating structure, effectively minimising charge transfer and enhancing barrier properties.[66] Conversely, Pt-60 demonstrates the lowest R_{ct} (1390 Ω cm^2), indicative of a porous coating that allows greater electrolyte penetration and higher corrosion potential. The R_s values are consistently low across all samples, highlighting a minimal effect of electrolyte conductivity on the electrochemical responses. Pt-120 shows the highest double-layer capacitance (C_{dl} = 454.9 μF), supporting the presence of a compact barrier layer. Additionally, the CPE values, which address non-ideal capacitive behaviour due to surface roughness and coating inhomogeneity, vary among the samples. In terms of protective film resistance (R_{pfc}), Pt-120 also displays the highest value (1683 Ω cm^2), further supporting its superior corrosion protective capabilities. In the case of Pt(240), the intermediate R_{pfc} (518.5 Ω cm^2) and R_{ct} (2973 Ω cm^2) values suggest moderate corrosion resistance, likely compromised by microstructural defects or stress-induced cracks due to higher sputtering power.[67] Chronoamperometry (CA) further validates these findings by assessing long-term electrochemical stability at a constant applied potential *vs.* RHE over 15 hours under simulated anodic conditions. Fig. 4(d) illustrates the CA response of all samples. The steady-state current response follows the trend Pt-120

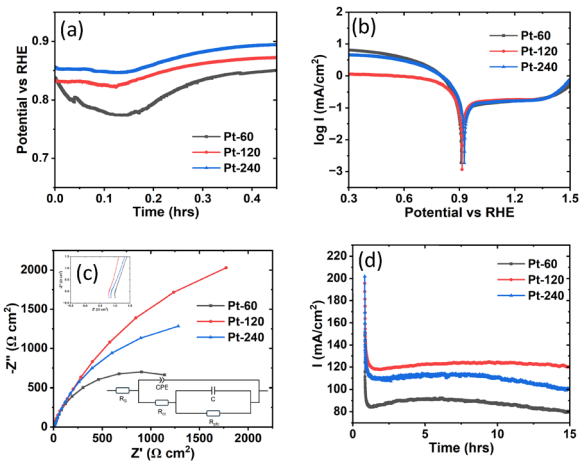

Fig. 4 (a) Open circuit potential (OCV), (b) potentiodynamic polarisation (c) Nyquist plot from EIS measured at OCV and the inset shows the equivalent circuit model and magnified high frequency region and (d) potentiostatic polarisation for 15 h at 2.0 V *vs.* RHE of the Pt-coated Ti-felt sample.

($120.8\ mA\ cm^{-2}$) > Pt-240 ($99.8\ mA\ cm^{-2}$) > Pt-60 ($80.1\ mA\ cm^{-2}$), indicating that Pt-120 maintains the most stable electrochemical behaviour with minimal charge transfer fluctuations, with strong catalytic activity for the OER.[20] Moreover, the initial fluctuations in current density may result from electrochemical cleaning, oxide layer erosion, and subsequent formation of a protective oxide layer.[68] Effective coatings exhibit rapid passivation, while less stable coatings display prolonged fluctuations due to continued oxide dissolution or incomplete passivation.[8] These electrochemical performance trends correlate directly with SEM (Fig. 2) and XRD findings (Fig. 3 and Table 1). The thick crystalline nature of Pt-240 yields the most positive OCV but higher grain boundaries and tensile strain create preferential sites for corrosion product to adhere and accelerate diffusion into the substrate, resulting in lower corrosion current, R_{pfc}, and long term stability.[69] Pt-60's open grain boundaries, partial coverage, and lower thickness cause faster degradation and inferior corrosion resistance. In contrast, Pt-120 exhibits a balanced grain structure with reduced grain boundaries, which minimises localised corrosion pathways and enhances passivation, resulting in durable films. Together, these results highlight the critical role of sputtering power in controlling film quality and electrochemical performance.

Evaluation of the TiN interlayer

Microstructure Pt-TiN coatings. Fig. 5 illustrates the X-ray diffraction (XRD) patterns of TiN-coated Ti-felt and Pt-coated TiN samples with interlayer thicknesses of 100 nm, 400 nm, and 700 nm. The diffraction peaks correspond to Ti and TiN phases (PDF No. 44-1294 and 38-1420, respectively).[70–72] Thin coatings allowed X-rays to penetrate the film, revealing coating and substrate diffraction peaks. The analysis shows distinct crystallographic changes with increasing TiN thickness, particularly in the (111) and (311) cubic phases at 2θ: 36.6° and 74.0°, respectively. Notably, the (311) peak diminishes as thickness increases, while the (111) phase sharpens, indicating a shift in preferred orientation. This trend aligns with prior studies on TiN films, where deposition conditions and stress mechanisms influence phase evolution. At lower thicknesses, TiN exhibits random orientations due to competitive nucleation. However, a strain-driven preferential orientation shift occurs with increasing thickness, favouring the (111) phase.[70] Moreover, after applying the topcoat from the best-performing configuration identified in the previous section, the XRD pattern of the Pt-120 coated TiN sample exhibits a similar trend to that described in the previous section, though with a significantly weaker signal from the TiN interlayer.

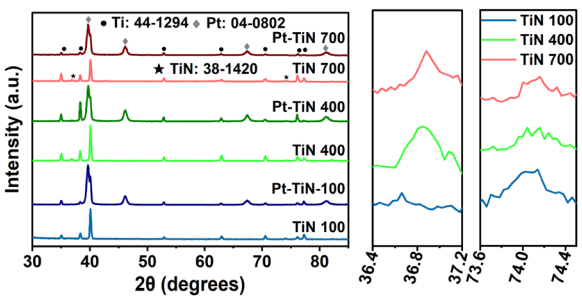

Fig. 5 (a) XRD pattern of three different thicknesses of TiN coatings with and without a Pt top layer. (b) Magnified view of TIN peaks.

Corrosion performance of Pt-coated Ti-felt PTLs with a TiN interlayer

The corrosion performance of Pt-coated Ti-felt with varying thicknesses of the TiN interlayer was comprehensively evaluated utilising OCV, Tafel polarisation, EIS, and CA analysis to ascertain electrochemical stability and resistance to degradation in acidic environments. The OCV analysis (Fig. 6(a)) revealed distinctive stabilisation trends across the samples, reflecting underlying differences in surface passivation behaviour and structural stability. The Pt-TiN-100 sample exhibited an initial OCV of 0.88 V, experiencing a rapid decline to 0.80 V within the first 10 min, followed by gradual recovery and stabilisation at approximately 0.83 V. This transient behaviour suggests incomplete surface passivation, likely due to partial coverage or insufficient thickness of the TiN interlayer, allowing Ti substrate exposure to the acidic medium. This can lead to localised electrochemical oxidation of Ti, forming non-protective TiO_2, which momentarily disrupts the electrode potential before stabilisation through repassivation. Contrarily, Pt-TiN-400 began at a relatively lower potential of 0.73 V, progressively increased to 0.88 V within 20 min, and eventually stabilised at 0.90 V. This upward trend indicates a more uniform defect-minimised interface that promotes effective passivation and electrochemical stability by delaying or suppressing initial Ti exposure. The gradual increase in potential reflects the development of a stable electrochemical interface as the Pt-TiN surface undergoes complete wetting and passivation under anodic conditions. Notably, Pt-TiN-700 exhibited significant instability with an initial sharp drop from 0.80 V to 0.48 V within 15 min, followed by recovery to 0.83 V and stabilising near 0.85V. This behavior may be attributed to internal stress or microstructural flaws in the thick TiN layer, which can

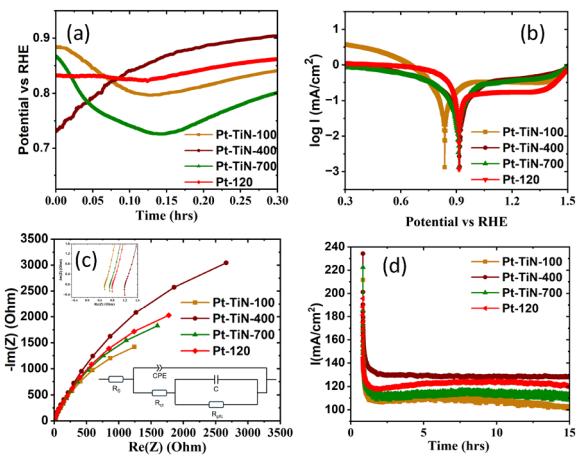

Fig. 6 (a) Open circuit potential (OCV), (b) potentiodynamic polarization, (c) Nyquist plot from EIS measured at OCV and inset showing equivalent circuit model and magnified high frequency region, and (d) potentiostatic polarization (for 15 h at 2.0 V *vs.* RHE) of the Pt-120 coated Ti-Felt sample with 100 nm, 400 nm and 700 nm thick TiN interlayers.

cause cracking, delamination, or delayed electrolyte penetration—leading to sudden potential drops as electrochemically active regions are exposed.[26,73] The eventual stabilisation suggests partial reformation of passive layers, but the initial instability highlights the performance limit of thick interlayers.

Tafel polarisation results (Fig. 6(b)) further elucidated corrosion kinetics, revealing a clear correlation between interlayer thickness and corrosion parameters. The Pt-TiN-400 demonstrated the lowest corrosion current density (I_{corr} = 39.26 μA cm^{-2}) coupled with the highest corrosion potential (E_{corr} = 0.915 V), indicative of superior corrosion resistance compared to the Pt-120 sample (I_{corr} = 41.1 μA cm^{-2}, E_{corr} = 0.913 V). Despite a comparable E_{corr} (0.907 V), the Pt-TiN-700 sample exhibited elevated corrosion current density (I_{corr} = 49.13 μA cm^{-2}), likely attributed to the introduction of structural inhomogeneities at higher interlayer thicknesses that promote localised degradation. Meanwhile, the Pt-TiN-100 sample showed the highest corrosion current density (I_{corr} = 55.45 μA cm^{-2}) and the lowest E_{corr} (0.839 V), signifying a pronounced tendency toward degradation over extended exposure. EIS analysis (Fig. 6(c)) provided deeper insights into interfacial phenomena through parameters such as charge transfer resistance (R_{ct}) and protective film integrity (R_{pfc}) (Table 4). Consistent with polarisation observations, Pt-TiN-400 exhibited the highest values for both R_{ct} (3552 Ω cm^2) and R_{pfc} (2306 Ω cm^2), suggesting a dense highly resistive barrier against corrosive species. Conversely, Pt-TiN-700 presented moderate R_{ct} (2131 Ω cm^2) and R_{pfc} (1384 Ω cm^2), while Pt-TiN-100 recorded the lowest values of R_{ct} (1657 Ω cm^2) and R_{pfc} (1076 Ω cm^2), underscoring the limited protective capacity and accelerated degradation kinetics. The diminished performance of Pt-TiN-700 is likely due to the presence of coarse grain boundaries, which act as preferential pathways for electrolyte penetration and subsequent corrosion.[74] Chronoamperometry over 15 hours under anodic bias also revealed distinct current stabilisation patterns, with measurements performed under simulated PEMWE conditions (three-electrode setup, 1.35 V *vs.* RHE, 0.5 M H_2SO_4, 70 °C) (Fig. 6(d)). All samples exhibited rapid initial declines before achieving steady-state conditions within approximately 15 min. The steady-state current density hierarchy was as follows: Pt-TiN-400 (128.7 mA cm^{-2}) > Pt-120 (120.1 mA cm^{-2}) > Pt-TiN-700 (110.8 mA cm^{-2}) > Pt-TiN-100 (101.9 mA cm^{-2}). Excessive thickness, as in Pt-TiN-700, can introduce stress-induced defects, grain boundary voids, and columnar grain growth—a factor known to compromise protective properties.[64,66] Thinner coatings (Pt-TiN-100) may lack sufficient barrier protection, leading to gradual degradation over time. While the Pt-TiN-400 sample features a moderate TiN thickness that effectively balances the structural integrity and electrochemical stability beyond that achieved by single-layer Pt-120 coatings and the other TiN variants. These results underscore a critical dependency of interlayer thickness on corrosion resistance. Furthermore, Fig. 7 presents the SEM and EDS results after 15 hours of CA. The SEM micrographs reveal film delamination with many fibers losing their coating in the Pt-TiN-700 and Pt-TiN-100 samples. In contrast, the Pt-TiN-400 sample exhibits a well-adhered and sustained coating, showing only minor delamination at substrate defect sites. These observations match the corrosion analysis and are further supported by the EDS derived atomic percentage of Pt, which are 27.1%, 55.8% and 25.7% in Pt-TiN-100, Pt-TiN-400 and Pt-TiN-700, respectively (see Fig. S5 for EDS mapping images).

Table 4 Equivalent circuit model parameters for PEIS analysis of Pt-coated Ti-felt with different thickness TiN interlayers

Sample	R_s (Ω cm^2)	R_{ct} (Ω cm^2)	R_{pfc} (Ω cm^2)
Pt-TiN-100	0.8027	1657	1076
Pt-TiN-400	0.9471	3552	2306
Pt-TiN-700	0.8597	2131	1384

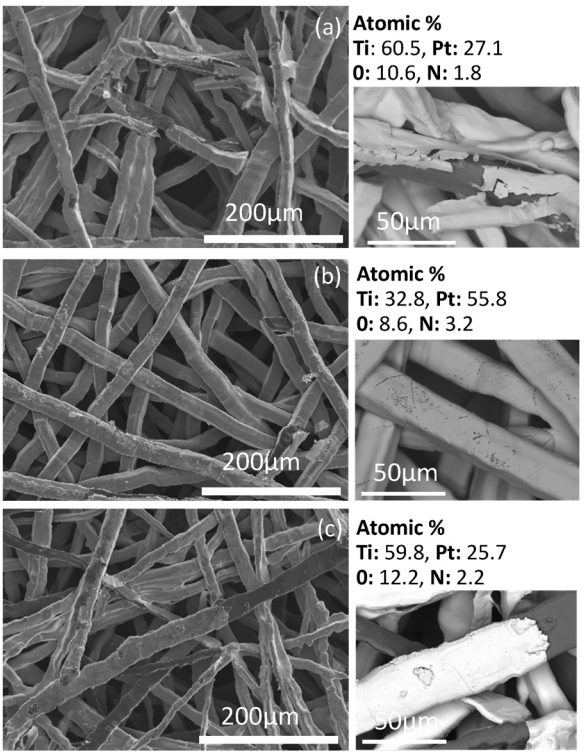

Fig. 7 SEM images of Pt-coated Ti-felt with the TiN interlayer after 15 h of CA (a) Pt-TiN-100, (b) Pt-TiN-400, and (c) Pt-TiN-700. Right side of each is the EDS results presenting the atomic % of the elements.

Ex situ lifetime testing of the coated Ti-felt PTLs

The coated Ti-felt samples were evaluated in an *ex situ* half-cell configuration for long-term stability of the coatings under conditions simulating a PEMWE environment. The test setup consisted of the coated Ti PTL (1 cm^2 active area) as the working electrode and a Pt wire as the counter electrode, immersed in 0.5 M H_2SO_4 at 70 °C. A constant current density of 1 A cm^{-2} was applied using a galvanostatic method, and the cell voltage was monitored continuously. Coating failure was defined by a sudden voltage rise exceeding 15 V, indicating electrochemical degradation and the development of an insulating TiO_x layer on the exposed Ti substrate. Fig. 8 illustrates the lifetime performance of the coatings. The Pt-TiN-400

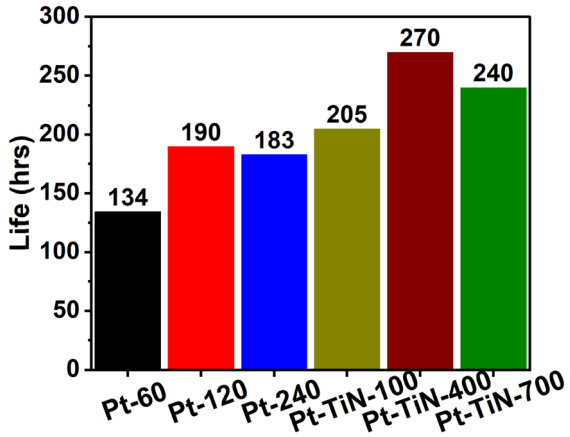

Fig. 8 Comparison of the lifetime performance of all the samples under accelerated operating conditions.

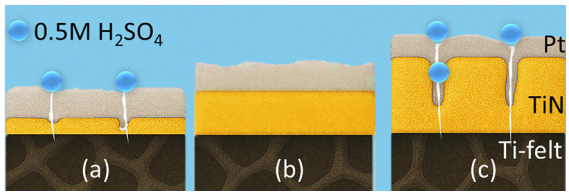

Fig. 9 (a) Pt-TiN-100 sample showing a thin TiN layer with incomplete coverage, leading to electrolyte penetration; (b) Pt-TiN-400 sample with a compact and uniform surface morphology; (c) Pt-TiN-700 sample exhibiting a thick columnar TiN layer prone to defects.

configuration exhibited the longest operational lifetime, outperforming both the single-layer Pt coatings (Pt-60, Pt-120, Pt-240) and the other bilayer samples (Pt-TiN-100 and Pt-TiN-700). This enhanced durability is attributed to the TiN interlayer, which provides effective coverage and promotes strong interfacial bonding with the Pt overlayer. The TiN-400 thickness appears to offer a balance, minimising residual stress while preserving interfacial integrity, thereby enhancing resistance to acidic degradation under sustained anodic polarisation. While increasing coating thickness is generally expected to improve corrosion resistance, the results reveal that excessively thick TiN layers (*e.g.*, TiN-700) can be detrimental. This behaviour is likely due to the formation of microstructural defects such as grain boundary voids, columnar discontinuities, and internal porosity, which act as diffusion pathways for electrolyte ingress as illustrated in Fig. 9. Penetration of oxygen and acidic species into these defects accelerates subsurface oxidation, disrupting the structural integrity around embedded microparticles and along columnar grain boundaries, which tend to proliferate with increased thickness. Consequently, leading to volume expansion, internal stress accumulation, and crack propagation. Such failure mechanisms compromise the protective function of the coating and shorten operational lifetime.[75,76]

In situ performance evaluation of TiN/Pt coated PTLs

Coated Ti PTLs were analysed through corrosion testing to determine the durability of the coating in acidic environments (0.5 M H_2SO_4), along with extended-duration trials to assess long-term performance in a controlled two-electrode simulation setup. Beyond performance evaluation in isolation, examining how the coated PTLs function under realistic operating parameters such as temperature, pressure, and interaction with electrolytes is critical. Real-time cell testing of the coated PTLs enables performance assessment in conjunction with other key components, such as the membrane electrode assembly (MEA) and bipolar plates, thereby confirming the coating's reliability in a fully functional electrolyser system.[26,54]

The polarisation curves were recorded through *in situ* electrochemical characterisation with Pt-coated Ti-felt (Pt-120), Pt-TiN-100, Pt-TiN-400, and Pt-TiN-700 PTLs using a PEMWE cell. The PTLs used in this study exhibited comparable pore structures, suggesting minimal variation in mass transport losses associated with oxygen evolution during single cell testing. As shown in Fig. 10(a), the Pt-TiN-400 configuration yielded improved current density–voltage (*I*–*V*) characteristics relative to the Pt-120, Pt-TiN-100, and Pt-TiN-700 samples. The polarisation data confirmed the high electrical conductivity of Pt-TiN-400 PTL owing to the well-formed interfacial contact between TiN and the Pt layer (Fig. S6). The optimal thickness of TiN-400 offered a balanced strain between the TiN and Pt layers. This structural synergy facilitated more effective electron transfer from Pt atoms into the TiN interlayer, resulting in increased local electron density. Enhanced electron mobility at this interface can be linked to the adsorption and desorption energies of reaction intermediates, supporting improved electrocatalytic performance under anodic polarization. The Pt-TiN-400 PTL exhibited a cell voltage of 1.755 V at 2.0 A cm^{-2} current density, surpassing values reported in recent studies.[16,25,77–81] The high ohmic resistances of the Pt-120, Pt-TiN-100 PTL, and Pt-TiN-700 PTL samples increased the cell potential to 1.842 V, 1.789 V, and 1.817 V, respectively, at 2.0 A cm^{-2}. It indicates that the oxidation of titanium fibres on the surface of the PTL resulted in the formation of Ti oxides in Pt-120 PTL and samples with minimal TiN thickness (Pt-TiN-100). The Pt-TiN-100 PTL, having a minimal TiN layer thickness, may be insufficient to fully cover the underlying titanium oxide present on the Ti fibres. The electrochemical performance trends observed in the PEMWE single-cell setup were consistent with the chronoamperometric responses recorded in acidic media using a three-electrode configuration (Fig. 6(d)).

The Pt-TiN-400 offered strong contact at the CL/PTL interface, thereby improving reaction kinetics and reducing high-frequency

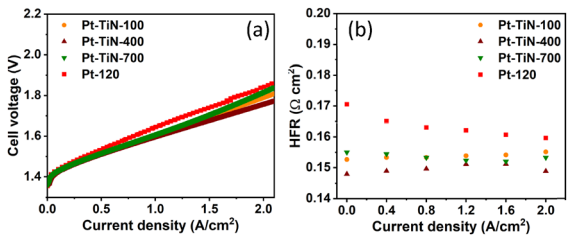

Fig. 10 (a) Polarisation curve, and (b) high frequency resistance (HFR) plots of Pt-120, Pt-TiN-100, Pt-TiN-400 and Pt-TiN-700 PTLs.

resistance (HFR). Typically, the HFR is an addition of electrical contact resistances and membrane resistance. Primarily, HFR comprises both electrical contact resistance and intrinsic resistance of the membrane.[23,77] In this study, membrane resistance remained constant across all four PTL samples, given the uniform MEA specifications. The applied coatings increased the effective electrically conductive area in contact with the catalyst layer while preventing MEA deformation under compression. The Pt-TiN-400 offered superior catalyst utilisation in PEMWE as compared to without the TiN (Pt-120), Pt-TiN-100 PTL, and Pt-TiN-700 PTL, as shown in Fig. 9(b), EIS was used to record HFR values across different current densities. Among the tested samples, Pt-TiN-400 exhibited the lowest and almost constant HFR values across the current density range (0.4–2.0 A cm^{-2}). In contrast, the Pt-120, Pt-TiN-100 PTL, and Pt-TiN-700 PTL samples exhibited higher HFR at similar current densities. The high HFR value of the Pt-120 and Pt-TiN-100 PTL samples may be attributed to the presence of a passivated TiO_x layer on the Ti PTL. Additionally, the thick 700 nm TiN layer may induce interfacial stress at the TiN/Pt interface, further increasing the PEMWE cell's HFR. It can be concluded that the optimal interlayer of TiN-400 coating has significantly enhanced electrical contact at the CL/PTL interface.

Comparative analysis unequivocally demonstrates that incorporating TiN interlayers significantly enhances corrosion resistance and durability of Pt-coated Ti-felt, paving a path to lower the operational cost[82] and to reduce noble metal expenses. Moreover, highlighting the necessity for optimisation of the TiN interlayer characteristics, particularly thickness, stoichiometry, and structural homogeneity, which vary significantly with manufacturing routes.[33] Hence, achieving optimal performance requires balancing process parameters, coating thickness, microstructure, and stress management to minimise defects and enhance durability.

Conclusions

This study establishes the critical role of TiN interlayers in enhancing the electrochemical stability and corrosion resistance of the Pt-coated Ti-PTL for PEMWE. Initial evaluation of Pt sputtering conditions identified the Pt-120 configuration as the most stable, offering a compact grain morphology with reduced residual strain and improved film continuity. Subsequent integration of TiN interlayers with controlled thicknesses (100, 400, and 700 nm) demonstrated a strong correlation between interlayer thickness and long-term performance. Among these, the Pt-TiN-400 sample exhibited the best results, achieving the lowest corrosion current density (I_{corr} = 39.26 μA cm^{-2}), increased charge transfer resistance ($\sim$3552 Ω cm^2), and superior interfacial stability under prolonged anodic stress. Lifetime testing confirmed that Pt-TiN-400 extended operational stability by 80 hours compared to non-interlayered samples. Furthermore, single-cell PEMWE evaluations revealed reduced high-frequency resistance and improved impedance response, indicating more stable interfacial contact. These findings highlight the impact of TiN interlayers in mitigating Ti substrate passivation, suppressing oxide formation, and maintaining electrochemical performance during extended operation. A moderately thick TiN interlayer, such as the 400 nm configuration, was shown to balance internal stress while preserving coating integrity. This work presents a viable materials design strategy for improving the durability and operational performance of PEMWE PTLs, underscoring the potential of thin-film interfacial engineering for next-generation water electrolysis systems.

Author contributions

Muhammad Azhar Iqbal: writing – original draft, formal analysis, investigation, methodology, and visualization. Sukhvant Singh: investigation, validation, review, and editing. Aditya Singh: data curation, formal analysis, validation, review, and editing. Samaneh Shahgaldi: project administration, resources, supervision, validation, review, and editing.

Conflicts of interest

There are no conflicts to declare.

Data availability

All data reported in this study were generated by the authors and are securely stored within the research group facilities at the University of Quebec at Trois-Rivières (UQTR), Canada. Comprehensive characterization data are included within the main article and supplementary file. Additional data supporting the findings are available from the corresponding authors upon reasonable request.

Supplementary information (SI) is available. See DOI: https://doi.org/10.1039/d5ma01378j.

Acknowledgements

This research was supported by Mitacs Accelerate (Application Ref.: IT29926) in collaboration with Intlvac Canada, as well as by the Natural Sciences and Engineering Research Council of Canada (NSERC), Canada Research Chair (CRC-2019-00354), and Discovery Grant (CRSNG-DGECR-2022-00058).

References

1 IEA, Global Hydrogen Review 2024, IEA, Paris, 2024.
2 IEA, Global Hydrogen Review 2025, Paris, 2025.
3 A. W. Tricker, T. Y. Ertugrul, J. K. Lee, J. R. Shin, W. Choi, D. I. Kushner, G. Wang, J. Lang, I. V. Zenyuk, A. Z. Weber and X. Peng, *Adv. Energy Mater.*, 2024, **14**, 2303629.
4 C. Liu, J. A. Wrubel, E. Padgett and G. Bender, *Appl. Energy*, 2024, **356**, 122274.
5 DoE, Hydrogen Shot, Department of Energy.
6 IEA, The Future of Hydrogen, OECD, 2019.
7 H. Tüysüz, *Acc. Chem. Res.*, 2024, **57**, 558–567.

8 M. Johar, L. Moradizadeh, A. Gupta, Y. Mehdizadeh Chellehbari, X. Li and S. Shahgaldi, *Corros. Sci.*, 2025, **245**, 112707.
9 S. Shiva Kumar and H. Lim, *Energy Rep.*, 2022, **8**, 13793–13813.
10 A. Kellenberger, N. Vaszilcsin, D. Duca, M. L. Dan, N. Duteanu, S. Stiber, T. Morawietz, I. Biswas, S. A. Ansar, P. Gazdzicki, F. J. Wirkert, J. Roth, U. Rost, M. Brodmann, A. S. Gago and K. A. Friedrich, *Materials*, 2022, **15**, 1628.
11 S. Schlicht, K. Percin, S. Kriescher, A. Hofer, C. Weidlich, M. Wessling and J. Bachmann, *Beilstein J. Nanotechnol.*, 2020, **11**, 952–959.
12 C. Van Pham, D. Escalera-López, K. Mayrhofer, S. Cherevko and S. Thiele, *Adv. Energy Mater.*, 2021, **11**, 2101998.
13 L. Moradizadeh, P. Varsan, Y. Mehdizadeh, A. Gupta, X. Li and S. Shahgaldi, *Int. J. Hydrogen Energy*, 2024, **94**, 1114–1129.
14 S. Zaman, M. Khalid and S. Shahgaldi, *ACS Energy Lett.*, 2024, **9**, 2922–2935.
15 A. Ghadbane, X. Z. Yuan, A. Platt, A. Malek, N. Shaigan, M. Dinu, S. Shahgaldi and K. Fatih, *A Review of Diagnostic Tools for Evaluating Porous Transport Layers for Proton Exchange Membrane (PEM) Water Electrolysis*, Springer Nature Singapore, 2025, vol. 8.
16 Z. Fan, H. Yu, G. Jiang, D. Yao, S. Sun, J. Chi, B. Qin and Z. Shao, *Int. J. Hydrogen Energy*, 2022, **47**, 18963–18971.
17 J. Mo, S. M. Steen, B. Han, Z. Kang, A. Terekhov, F. Y. Zhang, S. T. Retterer and D. A. Cullen, in 13th International Energy Conversion Engineering Conference, American Institute of Aeronautics and Astronautics, Reston, Virginia, 2015, pp. 1–9.
18 N. F. Daudt, A. D. Schneider, E. R. Arnemann, C. J. Scheuer, L. S. Dorneles and L. F. Schelp, *J. Mater. Eng. Perform.*, 2020, **29**, 5174–5183.
19 Z. Kang, T. Schuler, Y. Chen, M. Wang, F. Y. Zhang and G. Bender, *Electrochim. Acta*, 2022, **429**, 140942.
20 A. Gupta, Y. M. Chellehbari and S. Shahgaldi, *J. Power Sources*, 2025, **630**, 236088.
21 Anurag, A. Gupta and S. Shahgaldi, *Electrochim. Acta*, 2025, **538**, 147053.
22 R. Zhang, Q. Y. Ma, H. Liu, T. Y. Sun, J. Bi, Y. Song, S. Peng, L. Liang, J. Gao, H. Cao, L. F. Huang and Y. Cao, *ACS Photonics*, 2021, **8**, 847–856.
23 C. Liu, M. Shviro, A. S. Gago, S. F. Zaccarine, G. Bender, P. Gazdzicki, T. Morawietz, I. Biswas, M. Rasinski, A. Everwand, R. Schierholz, J. Pfeilsticker, M. Müller, P. P. Lopes, R. A. Eichel, B. Pivovar, S. Pylypenko, K. A. Friedrich, W. Lehnert and M. Carmo, *Adv. Energy Mater.*, 2021, **11**, 2002926.
24 T. Bautkinova, N. Utsch, T. Bystron, M. Lhotka, M. Kohoutkova, M. Shviro and K. Bouzek, *J. Power Sources*, 2023, **565**, 232913.
25 C. Liu, M. Carmo, G. Bender, A. Everwand, T. Lickert, J. L. Young, T. Smolinka, D. Stolten and W. Lehnert, *Electrochem. commun.*, 2018, **97**, 96–99.
26 A. Singh, B. S. De, S. Singh, S. P. Thota, M. Khalid and S. Shahgaldi, *Int. J. Hydrogen Energy*, 2025, **106**, 1029–1040.
27 P. Varsan Madhavan, S. Shahgaldi and X. Li, *Energy Convers. Manag.*, 2024, **311**, 118536.
28 S. Singh, A. Singh, M. A. Iqbal and S. Shahgaldi, *Energy Adv.*, 2026, **5**, 56–70.
29 H. Kim, K.-R. Yeo, H.-Y. Park, J. H. Jang and S.-K. Kim, *Korean J. Chem. Eng.*, 2025, **42**, 3365–3378.
30 C. Rakousky, U. Reimer, K. Wippermann, M. Carmo, W. Lueke and D. Stolten, *J. Power Sources*, 2016, **326**, 120–128.
31 L. Moradizadeh, P. V. Madhavan, A. Ozden, X. Li and S. Shahgaldi, *Energy Convers. Manag.*, 2025, **332**, 119713.
32 T. Bystron, M. Vesely, M. Paidar, G. Papakonstantinou, K. Sundmacher, B. Bensmann, R. Hanke-Rauschenbach and K. Bouzek, *J. Appl. Electrochem.*, 2018, **48**, 713–723.
33 L. Stein, A. Dittrich, D. C. Walter, P. Trinke, B. Bensmann and R. Hanke-Rauschenbach, *ACS Appl. Mater. Interfaces*, 2025, **17**, 19070–19085.
34 T. L. Doan, T. N. Nguyen, Y. S. Jung, C. Lee, M. J. Kim, S. Lee, H. S. Cho and T. Kim, *Int. J. Hydrogen Energy*, 2024, **55**, 839–847.
35 Z. Fan, H. Yu, G. Jiang, D. Yao, S. Sun, J. Chi, B. Qin and Z. Shao, *Int. J. Hydrogen Energy*, 2022, **47**, 18963–18971.
36 M. Forouzanmehr, K. R. Kashyzadeh, A. Borjali, A. Ivanov, M. Jafarnode, T. H. Gan, B. Wang and M. Chizari, *Sensors*, 2022, **22**, 750.
37 S. Pugal Mani, A. Srinivasan and N. Rajendran, *Int. J. Hydrogen Energy*, 2015, **40**, 3359–3369.
38 Y. Jang, Y. Kim, W. Jeong, S. Ko, D. Gil, I. Jeong, M. S. Lee, S. Ryu, K. H. Jang and S. W. Cha, *J. Alloys Compd.*, 2024, **977**, 173379.
39 W. M. Yan, J. C. Lin, C. Y. Chen and M. Amani, *Renew. Energy*, 2023, **216**, 119042.
40 H. Ye, Z. Tu and S. Li, *J. Power Sources*, 2024, **595**, 234052.
41 S. I. Butrim, M. A. Solovyev, I. V. Pushkareva, V. V. Tishkin, D. A. Simkin, B. L. Shapir, M. V. Kozlova, O. K. Alekseeva, E. V. Kukueva, A. S. Pushkarev and V. N. Fateev, *Nanobiotechnol. Rep.*, 2023, **18**, S367–S374.
42 D. Zhang, L. Duan, L. Guo, Z. Wang, J. Zhao, W.-H. Tuan and K. Niihara, *Int. J. Hydrogen Energy*, 2011, **36**, 9155–9161.
43 W. J. Lee, E. Y. Yun, H. B. R. Lee, S. W. Hong and S. H. Kwon, *Appl. Surf. Sci.*, 2020, **519**, 146215.
44 A. Minoura, M. Kumagai, H. Yashiro, H. Okabe, H. Michibata and M. Murase, *Electrochemistry*, 2025, 62–67.
45 J. Gao, X. Wang, K. Liu, J. Ning, Y. Lv, J. Chen, Y. Wang and F. Ma, *Appl. Surf. Sci. Adv.*, 2025, **30**, 100865.
46 Z. Wang, B. Zhang, K. Gao and R. Liu, *Int. J. Hydrogen Energy*, 2022, **47**, 39215–39224.
47 Y. Tao, M. Wu, M. Hu, X. Xu, M. I. Abdullah, J. Shao and H. Wang, *SusMat*, 2024, **4**, e230.
48 S. A. G. Evans, J. G. Terry, N. O. V. Plank, A. J. Walton, L. M. Keane, C. J. Campbell, P. Ghazal, J. S. Beattie, T. J. Su, J. Crain and A. R. Mount, *Electrochem. Commun.*, 2005, **7**, 125–129.
49 A. Ostroverkh, V. Johánek, M. Dubau, P. Kúš, I. Khalakhan, B. Šmíd, R. Fiala, M. Václavů, Y. Ostroverkh and V. Matolín, *Int. J. Hydrogen Energy*, 2019, **44**, 19344–19356.
50 A. Villamayor, D. Galyamin, L. V. Barrio, E. G. Berasategui and S. Rojas, *Int. J. Hydrogen Energy*, 2024, **64**, 50–57.
51 Y. Mehdizadeh Chellehbari, P. V. Madhavan, M. Johar, L. Moradizadeh, A. Gupta, X. Li and S. Shahgaldi, *eTransportation*, 2025, **26**, 100500.

52 O. K. Ozdemir, *Electrochemistry*, 2015, **83**, 76–79.
53 Q. Wang, Z. Zhou, K. Ye, M. Hu, X. Hu, S. Wang and C. Hu, *Int. J. Hydrogen Energy*, 2024, **53**, 163–172.
54 S. Singh, A. Singh, M. A. Iqbal and S. Shahgaldi, *Int. J. Hydrogen Energy*, 2025, **157**, 150478.
55 X. Fu, S. Guo, Y. Wan, Q. Li, B. Liu and H. Zheng, *Coatings*, 2022, **13**(1), 78.
56 A. J. Bard and L. R. Faulkner, Electrochemical Methods: Fundamentals and Applications, 2001.
57 S. Niu, S. Li, Y. Du, X. Han and P. Xu, *ACS Energy Lett.*, 2020, **5**, 1083–1087.
58 M. Schönleber, D. Klotz and E. Ivers-Tiffée, *Electrochim. Acta*, 2014, **131**, 20–27.
59 B. A. Boukamp, *J. Electrochem. Soc.*, 1995, **142**, 1885–1894.
60 E. Kuhnert, V. Hacker and M. Bodner, *Int. J. Energy Res.*, 2023, **2023**, 3183108.
61 M. Azhar, I. Zuhair, S. K. Nisar and A. Asghar, *Arab. J. Sci. Eng.*, 2021, **46**, 761–768.
62 N. Ahmed, Z. S. Khan and A. Ali, *Appl. Phys. A Mater. Sci. Process.*, 2022, **128**, 1–13.
63 J. Huang, S. Zou, W. Xiao, X. Liu and D. Tang, *Mater. Res. Express*, 2020, **7**(10), 106402.
64 J. Yang, K. Zhao, G. Wang, C. Deng, N. Liu, W. Zhang and J. Yang, *Surf. Coat. Technol.*, 2022, **441**, 128502.
65 Y. Mehdizadeh Chellehbari, A. Gupta, X. Li and S. Shahgaldi, *Molecules*, 2024, **29**, 4319.
66 J. H. Huang, F. Y. Ouyang and G. P. Yu, *Surf. Coatings Technol.*, 2007, **201**, 7043–7053.
67 Z. Gao, D. Yang, C. Sun, L. Du, X. Zhang and Z. An, *Metals*, 2021, **11**, 1522.
68 G. Liu, D. Shan, B. Fang and X. Wang, *Int. J. Hydrogen Energy*, 2023, **48**, 18996–19007.
69 P. Wang, L. Ma, X. Cheng and X. Li, *Int. J. Miner. Metall. Mater.*, 2021, **28**(7), 1112–1126.
70 E. Ajenifuja, A. Patricia, I. Popoola and O. M. Popoola, *Integr. Med. Res.*, 2018, **8**, 377–384.
71 M. Ahmed, N. Ahmed, H. Ahmad, S. Bashir, R. Subramaniam and G. Ali, *J. Energy Storage*, 2025, **105**, 114712.
72 X. Wang, J. Zou, Z. Zhang, C. Zhao, M. Wang and M. Wu, *Fuel*, 2025, **381**, 133559.
73 S. Dubent and A. Mazard, *Int. J. Hydrogen Energy*, 2019, **44**, 15622–15633.
74 J. Vega, H. Scheerer, G. Andersohn and M. Oechsner, *Corros. Sci.*, 2018, **133**, 240–250.
75 M. Zhang, Y. Niu, L. Xin, J. Su, Y. Li, T. Wu, H. Zhao, Y. Zhang, W. Xie, S. Zhu and F. Wang, *Ceram. Int.*, 2020, **46**, 19274–19284.
76 H. Tao, V. Zhylinski, A. Vereschaka, V. Chayeuski, H. Yuanming, F. Milovich, C. Sotova, A. Seleznev and O. Salychits, *Coatings*, 2023, **13**, 750.
77 C. Liu, K. Wippermann, M. Rasinski, Y. Suo, M. Shviro, M. Carmo and W. Lehnert, Constructing a Multifunctional Interface between Membrane and Porous Transport Layer for Water Electrolyzers, 2021, vol. 13.
78 C. Rakousky, G. P. Keeley, K. Wippermann, M. Carmo and D. Stolten, *Electrochim. Acta*, 2018, **278**, 324–331.
79 S. A. Grigoriev, P. Millet, S. A. Volobuev and V. N. Fateev, *Int. J. Hydrogen Energy*, 2009, **34**, 4968–4973.
80 M. Yasutake, Z. Noda, J. Matsuda, S. M. Lyth, M. Nishihara, K. Ito, A. Hayashi and K. Sasaki, *Int. J. Hydrogen Energy*, 2024, **49**, 169–183.
81 J. O. Majasan, F. Iacoviello, P. R. Shearing and D. J. L. Brett, *Energy Procedia*, 2018, **151**, 111–119.
82 H. Ye, L. Chen, D. Shen, S. Li and Z. Tu, *Int. J. Hydrogen Energy*, 2024, **93**, 1022–1030.